

Kilonova Light Curves from the Disk Wind Outflows of Compact Object Mergers

Daniel Kasen^{1,2,3}, Rodrigo Fernández^{1,2}, Brian D. Metzger⁴

¹ Department of Astronomy and Theoretical Astrophysics Center, University of California, Berkeley, CA 94720, USA.

² Department of Physics, University of California, Berkeley, CA 94720, USA.

³ Nuclear Science Division, Lawrence Berkeley National Laboratory, Berkeley, CA 94720, USA.

⁴ Columbia Astrophysics Laboratory, Columbia University, New York, NY 10027, USA.

Submitted to MNRAS

ABSTRACT

We study the radioactively-powered transients produced by accretion disk winds following a compact object merger. Starting with the outflows generated in two-dimensional hydrodynamical disk models, we use wavelength-dependent radiative transfer calculations to generate synthetic light curves and spectra. We show that the brightness and color of the resulting *kilonova* transients carry information about the merger physics. In the regions of the wind where neutrino irradiation raises the electron fraction to $Y_e \gtrsim 0.25$, r-process nucleosynthesis halts before producing high-opacity, complex ions (the lanthanides). The kilonova light curves thus show two distinct components: a brief (~ 2 day) blue optical transient produced in the outer lanthanide-free ejecta, and a longer (~ 10 day) infrared transient produced in the inner, lanthanide line-blanketed region. Mergers producing a longer-lived neutron star, or a more rapidly spinning black hole, have stronger neutrino irradiation, generate more lanthanide-free ejecta, and are optically brighter and bluer. At least some optical emission is produced in all disk wind models, which should enhance the detectability of electromagnetic counterparts to gravitational wave sources. However, the presence of even a small amount ($10^{-4} M_\odot$) of overlying, neutron-rich dynamical ejecta will act as a “lanthanide-curtain”, obscuring the optical wind emission from certain viewing angles. Because the disk outflows have moderate velocities ($\sim 10,000$ km s⁻¹), numerous resolved line features are discernible in the spectra, distinguishing disk winds from fast-moving dynamical ejecta, and offering a potential diagnostic of the detailed composition of freshly produced r-process material.

Key words: gravitational waves — gamma-ray burst: general — hydrodynamics — nuclear reactions, nucleosynthesis, abundances — opacity — radiative transfer

1 INTRODUCTION

The ejection of radioactive material during, or immediately following, the merger of two neutron stars (or a neutron star and a black hole) can give rise to an optical/infrared transient similar to, but dimmer and briefer than, an ordinary supernova (Li & Paczyński 1998; Kulkarni 2005; Metzger et al. 2010; Roberts et al. 2011; Barnes & Kasen 2013; Piran et al. 2013; Tanaka & Hotokezaka 2013; Grossman et al. 2014; Tanaka et al. 2014). These transients, called *kilonovae*, are promising electromagnetic counterparts to gravitational wave sources (Metzger & Berger 2012; Nissanke et al. 2013), and may be diagnostic of the sites of heavy element nucleosynthesis (Lattimer & Schramm 1974; Freiburghaus et al. 1999; Goriely et al. 2011; Piran et al. 2014).

Most studies of kilonovae have focused on material that becomes unbound during the merger itself. Simulations find that, on a dynamical timescale of \sim milliseconds, around $10^{-4} - 10^{-2} M_\odot$ of material may be flung out from the tips of the tidal tails or squeezed out from the contact interface between the two coalescing stars (e.g., Rosswog 2005; Duez et al. 2010; Hotokezaka et al. 2013; Bauswein et al. 2013). This dynamical ejecta is initially very neutron rich, with an electron fraction $Y_e = n_p/(n_n + n_p) \lesssim 0.1$, where n_p and n_n are the number density of protons and neutrons, respectively. Neutrinos emitted by the hot merger remnant can irradiate the outflowing material, perhaps raising the $Y_e > 0.1$ along the polar rotation axis (Wanajo et al. 2014).

Recently, more attention has focused on the possibil-

Table 1. Disk wind model properties and summary of radiative transfer results. The first two columns from the left show model name and lifetime of the HMNS, respectively. The following five columns show properties of the homologous ejecta: mass with $Y_e < 0.25$, mass with $Y_e > 0.25$, kinetic energy, mean velocity of material with $Y_e < 0.25$, and mean velocity of material with $Y_e > 0.25$. The last three columns give the peak luminosities in the blue (3500 – 5000 Å), red (5000 – 7000 Å), and infrared (1 – 3 μ m) bands, respectively.

Model	t_{ns} (ms)	$M_{Y_e < 0.25}$ (M_\odot)	$M_{Y_e > 0.25}$ (M_\odot)	KE ergs	$\bar{v}_{Y_e < 0.25}$ (km s $^{-1}$)	$\bar{v}_{Y_e > 0.25}$ (km s $^{-1}$)	$\nu L_\nu(\text{B})$ (ergs/sec)	$\nu L_\nu(\text{R})$ (ergs/sec)	$\nu L_\nu(\text{IR})$ (ergs/sec)
t000	0	1.5×10^{-3}	6.9×10^{-5}	1.6×10^{48}	8,927	18,583	4.3×10^{40}	2.1×10^{40}	8.5×10^{39}
t030	30	2.7×10^{-3}	5.4×10^{-4}	9.9×10^{48}	7,424	29,518	5.8×10^{40}	6.0×10^{40}	1.0×10^{40}
t100	100	7.3×10^{-4}	5.3×10^{-3}	2.5×10^{49}	9,805	15,007	6.6×10^{40}	1.3×10^{41}	5.7×10^{39}
t300	300	-	1.5×10^{-2}	6.9×10^{49}	-	16,432	8.5×10^{40}	2.4×10^{41}	1.2×10^{40}
tInf	∞	-	2.9×10^{-2}	1.9×10^{50}	-	21,419	2.7×10^{41}	3.9×10^{41}	2.0×10^{40}
a0.8	0	4.9×10^{-3}	8.4×10^{-4}	9.9×10^{48}	9,996	21,012	1.3×10^{41}	7.5×10^{40}	2.1×10^{40}

ity that a comparable or greater amount of mass may be expelled subsequent to the merger, as material in a rotationally supported disk accretes onto the central remnant on a viscous timescale (~ 1 s) (e.g., Metzger et al. 2008; Beloborodov 2008; Metzger et al. 2009). Viscous and nuclear heating during accretion can drive winds that unbind a significant fraction of the disk (Lee et al. 2009; Fernández & Metzger 2013a; Just et al. 2014). Neutrino irradiation during this phase will change the composition of the outflows. If the central remnant is a black hole (BH), neutrinos emitted from the inner region of the disk will raise the mean electron fraction of the wind to $Y_e \sim 0.2$ (Surman et al. 2006; Metzger & Fernández 2014). If the BH is rapidly spinning, this neutrino irradiation is enhanced, leading to higher values of Y_e (Just et al. 2014; Fernández et al. 2014). If the central remnant survives for some period of time as a hyper-massive neutron star (HMNS) before collapsing to a BH, the neutrino irradiation will be even stronger, and the electron fraction can be raised to yet higher values, $Y_e \sim 0.3$ (Metzger & Fernández 2014; Perego et al. 2014).

The value of Y_e in large part determines the final composition of the ejecta, and has a dramatic effect on the kilonova light curves. Unbound material will assemble into heavy elements via rapid neutron captures, or the r-process. The line opacity of some heavy elements differs significantly from that of ordinary astrophysical mixtures. In particular, for species with open f -shell valence electron configurations, namely the lanthanides (atomic number $Z = 58 - 70$) and actinides ($Z = 89 - 103$), the high atomic complexity leads to extremely high opacities (Kasen et al. 2013). The high lanthanide opacity leads to a dimmer, longer-duration kilonova light curve with emission peaking at infrared, rather than optical, wavelengths (Barnes & Kasen 2013).¹

For ejecta with low electron fraction, r-process nucleosynthesis proceeds all the way up to the third r-process peak, and a significant fraction of lanthanides, and perhaps actinides (Eichler et al. 2014), are produced. For higher electron fraction, nucleosynthesis stops at the second r-process peak, and the ejecta remains lanthanide-free. The color and brightness of kilonova light curves are therefore sensitive

markers of the electron fraction of the ejecta, and can be used to gain insight into the physics of compact object mergers.

The predicted colors of disk winds will also impact strategies for finding electromagnetic counterparts to the gravitational wave sources detected by the advanced LIGO/VIRGO experiments. Most existing and upcoming wide-field surveys observe in optical bands; infrared surveys are less common and typically have much lower sensitivity and a smaller field of view. The presence of optical emission from a lanthanide-free disk wind would therefore enhance the prospect of finding a kilonova.

Here we present radiative transfer calculations of kilonova light curves that allow us to connect the observables to the merger physics, e.g., the relative mass of dynamical to wind ejecta, the lifetime of a HMNS, or the spin of a central BH. We begin with the 2-dimensional hydrodynamical simulations from Metzger & Fernández (2014) and Fernández et al. (2014) which model the post-merger evolution (§2.1) and predict the distribution and electron fraction of unbound wind ejecta (§2.2). In addition, we carry out r-process reaction network calculations for parameterized wind outflows to estimate the critical electron fraction above which the ejecta is lanthanide free (§2.3). We then use a multi-dimensional radiative transfer code to generate synthetic kilonova spectra and light curves as a function of viewing angle (§3.1). We study several different models in order to explore the effects of the lifetime of a HMNS (§3.2), the spin of a BH (§3.3), and the presence of overlying dynamical ejecta (§3.4). We compare our wind light curves to observations of potential kilonova candidates (§3.5), and reflect on what implications our results have for detecting and interpreting kilonovae in the future (§4).

2 PROPERTIES OF DISK WINDS

2.1 Hydrodynamical Method

We consider six hydrodynamical disk wind simulations from Metzger & Fernández (2014) and one from Fernández et al. (2014), as shown in Table 1. All calculations begin with an equilibrium torus of mass $0.03 M_\odot$ surrounding a central remnant. Models differ in the amount of time that the neutron star survives before collapse to a black hole, with values of $t_{\text{ns}} = \{0, 30, 100, 300\}$ ms. For one model (tInf), the neutron star was assumed to survive indefinitely. All models assume a non-rotating black hole with the exception of model

¹ An important exception occurs if the outermost ejecta expands sufficiently rapidly for neutrons to avoid capture into nuclei. The high radioactive heating rate of free neutrons relative to r-process nuclei may power bright ultraviolet/blue emission on a timescale of hours following the merger, despite the presence of lanthanides (Metzger et al. 2014).

$a=0.8$, which considers the case of the prompt formation of a black hole with spin parameter $a = 0.8$. We constructed several additional ejecta models, discussed in §3.4, by superimposing an outer shell or torus of dynamical ejecta upon the wind model t100.

The hydrodynamical simulations use the FLASH3.2 code (Dubey et al. 2009), with modifications that enable modeling the viscous evolution of merger remnant accretion disks (Fernández 2012; Fernández & Metzger 2013a,b). The code includes a Helmholtz equation of state (Timmes & Swesty 2000) with abundances in nuclear statistical equilibrium, charged-current neutrino rates including emission from a hypermassive neutron star and disk self-irradiation via a neutrino leakage scheme, and viscous angular momentum transport via an α -viscosity prescription (Shakura & Sunyaev 1973). Approximate general relativistic effects are included via the pseudo-Newtonian potential of Paczyński & Wiita (1980) for non-spinning BHs and HMNSs, and the potential of Artemova et al. (1996) for the spinning BH case. All models are evolved until 3000 orbits at the initial density maximum, or ~ 10 s.

To follow the unbound ejecta all the way to free-expansion, we use a two-step process. First, in the original disk simulations we record all material leaving a sphere of radius 10^9 cm, centered on the central remnant. This information is then used as an inner boundary condition for a calculation on a new, larger computational domain of radius 10^{14} cm. The hydrodynamics are then carried out without any source terms other than gravity and the equation of state². The ambient density is reduced to 10^{-8} g cm⁻³ to prevent deceleration of the wind. By the time the ejecta reaches 10^{12} cm, the material is very nearly homologous, i.e., the kinetic energy dominates and the velocity is proportional to radius. From this time on, the dynamics can be extrapolated analytically.

2.2 Ejecta Properties

Figure 1 shows the density and compositional structure of a representative model, t030, in the homologous phase. The ejecta is approximately spherical, with the bulk of the material moving at speeds of $\sim 10,000$ km s⁻¹, or $0.03c$. Such expansion velocities are substantially lower than that of the dynamical ejecta, which moves at $0.1 - 0.3c$.

The outer layers of wind ejecta typically have a higher electron fraction than the inner regions, as the outer material is ejected at earlier times when the neutrino irradiation is higher due to the presence of a neutron star or a higher accretion rate onto the black hole. In model t030, a low Y_e plume is also seen along the equator. This feature forms out of the motion of the highly-irradiated component of the wind, which originates in regions of small radius and high altitude above the disk midplane, and wraps around the back of the disk with near north-south symmetry (Fernández et al. 2014). The mass in this plume, however, is very small compared to the spherical core.

Figure 2 shows, for each model, a histogram of the amount of mass ejected with various values of Y_e . Increasing

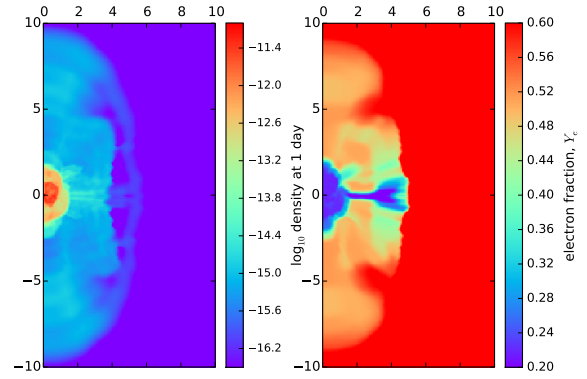


Figure 1. Density (left) and electron-fraction (right) structure of the ejecta from model t030 at 1 day after merger. In this phase, the ejecta is in homologous expansion, with velocity proportional to radius. The axes are given in velocity coordinates with units of 10^9 cm s⁻¹.

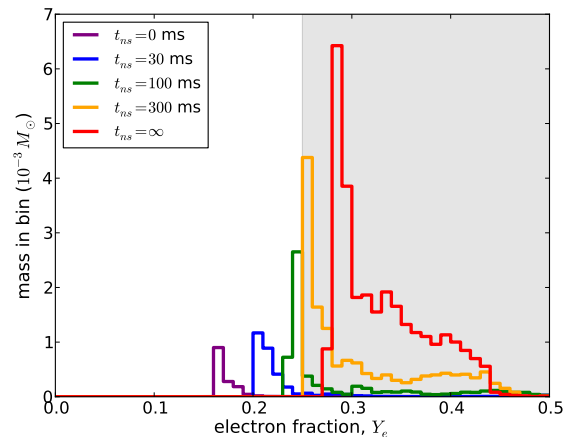


Figure 2. The amount of mass ejected with different values of the electron fraction, for disk wind models of different neutron star lifetimes, t_{ns} . A longer-lived neutron star leads to a larger total ejected mass and a higher mean electron fraction. The shaded area shows the region $Y_e > 0.25$ where the ejecta is likely lanthanide-free.

the lifetime of a HMNS has two main consequences. First, a larger total amount of mass is ejected, due to higher neutrino heating and the presence of a hard boundary at the HMNS, which keeps disk material from being swallowed below the event horizon of a BH. Second, the mean value of Y_e increases with t_{ns} due to the greater level of neutrino irradiation from both the HMNS and the disk.

2.3 Nucleosynthesis and Lanthanide Fraction

Knowledge of the compositional structure of the wind ejecta is needed to predict the resulting kilonova light curves. A full calculation of the ejecta abundances would require detailed nuclear-reaction network post-processing of thermodynamic

² Viscous and neutrino source terms operate on timescales slower than the expansion time at these radii.

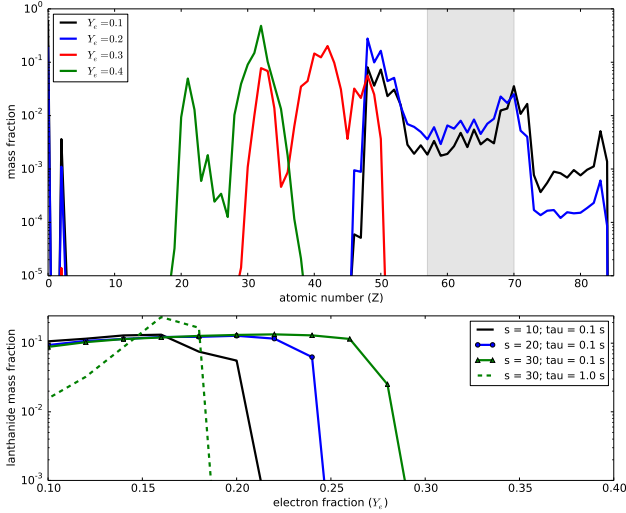


Figure 3. Nucleosynthesis results for parameterized wind models. *Top panel:* Final mass fractions of the wind for an expansion time $t = 0.1$ s, entropy $= 20 k_B/\text{baryon}$ and varying values of electron fraction, Y_e . For higher values of Y_e , the r-process fails to produce lanthanides (shaded grey region). *Bottom panel:* Integrated mass fraction of all lanthanides as a function of electron fraction assuming different values of entropy and expansion time. For conditions typical of disk wind ejecta ($s = 20 k_B/\text{baryon}$, $t = 0.1$ s), no lanthanides are produced if $Y_e \gtrsim 0.25$.

trajectories along the wind. Here we approximate the composition by a one-to-one mapping from the electron fraction. This mapping is obtained by evolving parameterized trajectories with the nuclear reaction network code Torch (Timmes 1999). Trajectories begin with abundances in nuclear statistical equilibrium at a temperature $T = 5 \times 10^9$ K and entropy $s \simeq 20 k_B/\text{baryon}$. The density decays exponentially in time, with expansion time $t_{\text{exp}} = 100$ ms and the entropy is held constant, assuming that radiation dominates the pressure. The chosen values of entropy and expansion time correspond to mass-flux weighted averages from disk wind simulations at the point where the average temperature is 5×10^9 K (Fernández & Metzger 2013a). Torch lacks a treatment of fission, which is an important physical effect in low- Y_e outflows, but should not be significant around the critical Y_e at which lanthanides first appear.

The top panel of Figure 3 shows the final mass fraction distributions for a few sample wind trajectories of different Y_e . We find that the lanthanide mass fraction decreases sharply above $Y_e \approx 0.25$. For electron fractions above this value, the neutron density is too low for the r-process to proceed past the long beta-decay lifetimes associated with the $N = 82$ closed shell nuclei, and nucleosynthesis halts at atomic numbers of $Z \approx 58$. For higher electron fractions, however, the flow is able to move past this point and proceeds rapidly to the next closed shell at $N = 126$.

The bottom panel of Figure 3 shows that the transition to a lanthanide-free composition is fairly abrupt in Y_e , and not overly sensitive to the value of the entropy chosen, so long as it is a few times $10 k_B/\text{baryon}$. We therefore consider $Y_e \approx 0.25$ as a critical value for distinguishing between the presence or absence of lanthanides.

3 LIGHT CURVES AND SPECTRA

3.1 Radiative Transfer Method

We input the homologous wind profiles from the hydrodynamical simulations of §2.2 into the multi-dimensional radiative transfer code Sedona (Kasen et al. 2006) to calculate synthetic light curves and spectra. The calculation setup was similar to that discussed in Kasen et al. (2013) and Barnes & Kasen (2013), and assumed local thermodynamic equilibrium for the atomic level populations and ionization state.

As the line data of high- Z elements is still incomplete, we used an approximate method to construct effective opacities of r-process mixtures. The opacity of all d-shell species was calculated using the atomic data for iron (Kurucz & Bell 1995), while the opacity of all f-shell species (the lanthanides) was calculated using the detailed atomic structure calculations for neodymium ($Z = 60$) (Kasen et al. 2013). Atomic structure calculations have shown that this proxy approach provides a reasonable approximation of the pseudo-continuum opacities, although it fails to produce the proper line features. We used the wind nucleosynthesis calculations of §2.3 to determine the abundance of lanthanides, and assumed that the remainder of the ejecta included the 30 d-shell species between $Z = 21$ and $Z = 80$.

For the radioactive heating rate, $\dot{\epsilon}_{\text{rad}}(t)$, of the wind, we use the results given in Roberts et al. (2011), which we assume to be the same in all regions of ejecta with $Y_e < 0.4$. In reality, the heating rate will depend on the local electron fraction. Grossman et al. (2014) show that, on day timescales, the heating rate of $Y_e \approx 0.1 - 0.3$ ejecta can be a factor of ~ 2 greater than that of the $Y_e < 0.1$ outflows calculated by Roberts et al. (2011). Our calculations may therefore underestimate the radioactive heating and kilonova luminosities. For $Y_e > 0.4$, the heating rate is lower (Grossman et al. 2014) and so we take $\dot{\epsilon}_{\text{rad}}(t) = 0$ in these regions. Since most of the ejecta have $Y_e < 0.4$, this choice has little impact on the final light curves.

The Sedona calculations generate the spectral time series every 0.1 days after merger, within a wavelength range of $200 - 30000 \text{ \AA}$, and from 20 different viewing angles equally spaced in the cosine of the polar angle θ . From the spectra, we constructed broadband light curves by averaging the emission over three different wavelength ranges: $3500 - 5000 \text{ \AA}$ (“blue”), $5000 - 7000 \text{ \AA}$ (“red”) and $1 - 3 \mu\text{m}$ (“infrared”). Table 1 gives the peak luminosity of all models in each of these bands.

3.2 Effect of Neutron Star Lifetime

Figure 4 shows the predicted light curves, from all viewing angles, of four models with different NS lifetimes. Figure 5 shows angle-averaged light curves for the same models. Because the wind outflows are roughly spherically symmetric, the variation of the light curves with viewing angle is generally small. The exception is model tInf, where the ejecta have a significant prolate elongation, and the blue light curve is a factor of ~ 3 brighter for an equatorial viewing angle, at which the projected surface area of the ejecta is maximal.

The light curves of model t000 – which assumes prompt formation of a BH – show two distinct components: a brief (~ 2 day) blue optical transient, and a longer (~ 10 day)

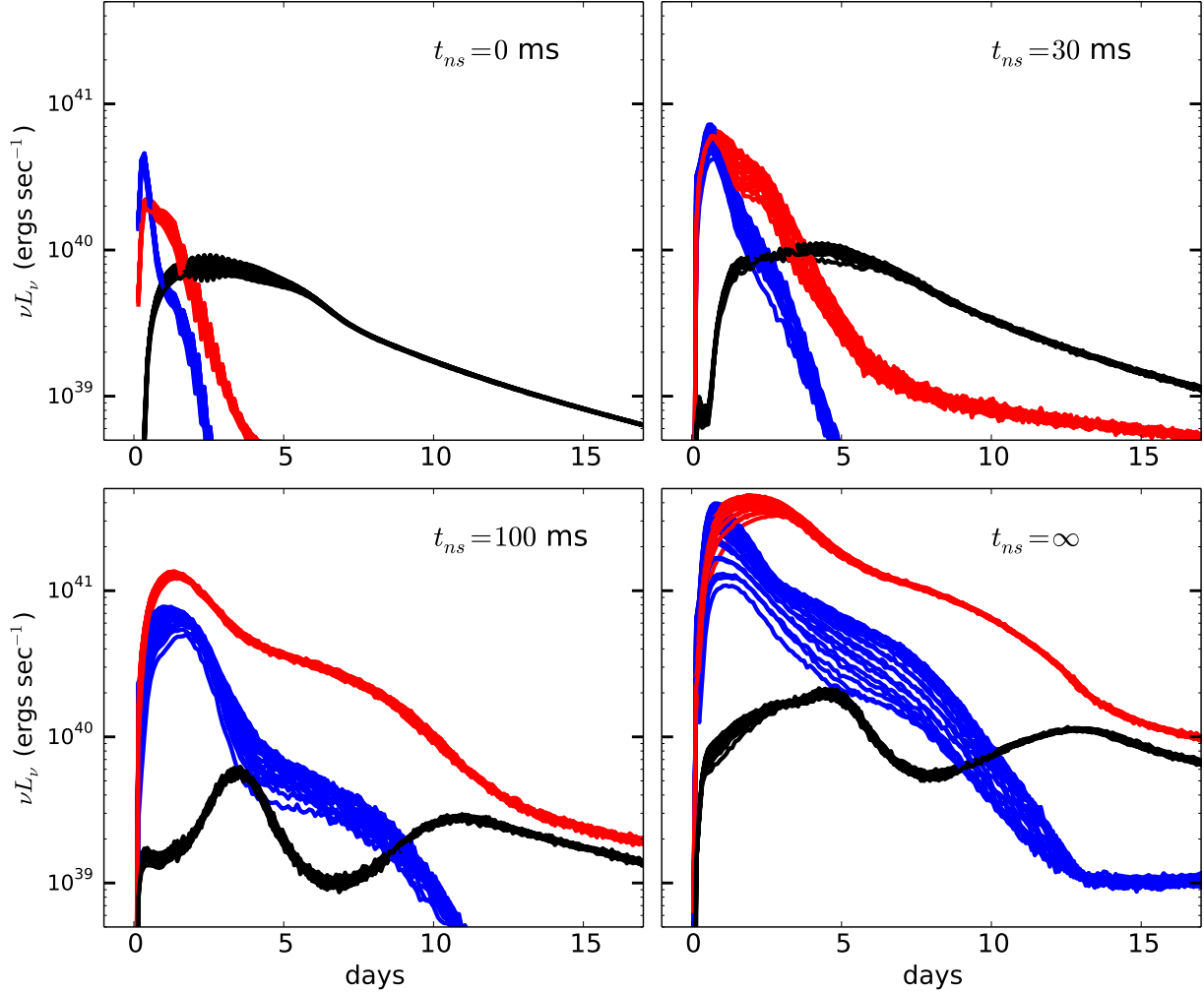


Figure 4. Synthetic light curves of models t000, t030, t100, and tInf. Blue lines denote blue optical emission (averaged over 3500–5000 Å), red lines denote red optical emission (5000–7000 Å), and black lines infrared emission (1–3 μm). Lines are overplotted for 20 different viewing angles, equally spaced in $\cos\theta$. A small amount of Monte Carlo noise is apparent in the calculations.

infrared transient. The infrared emission is generated within the central ejecta, where the electron fraction is $Y_e < 0.25$ and heavy line blanketing from the lanthanides suppresses the optical flux. This light curve is qualitatively similar to that found in the parameterized models calculated by Barnes & Kasen (2013). The blue component of the light curve is produced by the small amount of high Y_e (lanthanide-free) material in the outer layers of ejecta. The production of even a small ($\sim 10^{-4} M_\odot$) amount of high- Y_e in the exterior ejecta therefore has important implications for the detectability of kilonovae with optical facilities.

As the lifetime of the HMNS is increased, the optical light curves become brighter. This is because neutrino irradiation converts a larger fraction of the wind to $Y_e > 0.25$, and a greater total mass is ejected due to the hard boundary of the HMNS. For the extreme case of a stable NS (model tInf), the entire wind is lanthanide-free and the blue optical emission peaks at $\nu L_\nu \approx 2.8 \times 10^{41}$ ergs s $^{-1}$, a factor of 10 brighter than that of the prompt BH model t000. The optical light curves roughly follow analytic expectations that the duration should scale as $t \propto M^{-1/2}$ and the peak optical

luminosity as $L \propto M^{1/2}$ (Metzger et al. 2010), where M is the ejected mass of high Y_e material given in Table 1.

The dependence of the infrared brightness on t_{ns} is non-monotonic. The mass of low Y_e ejecta in model t030 ($t_{\text{ns}} = 30$ ms) is greater than that of model t000, and hence the infrared light curve brighter. A turnover point, however, is reached around $t_{\text{ns}} \approx 100$ ms, at which point the neutrino irradiation is sufficient to convert nearly the entire wind to high- Y_e , reducing the infrared emission. The kilonova colors thus correlate with the degree of neutrino irradiation. For $t_{\text{ns}} \lesssim 30$ ms, the ratio $\nu L_\nu(B)/\nu L_\nu(IR) \approx 5$, whereas for $t_{\text{ns}} > 30$ ms the color is much bluer, with $\nu L_\nu(B)/\nu L_\nu(IR) \approx 10$.

The origin of the infrared emission in models with $t_{\text{ns}} \gtrsim 100$ ms is distinct from those with $t_{\text{ns}} < 100$ ms. In the latter cases, the infrared emission arises in low- Y_e , lanthanide-blanketed regions of ejecta. In the former, there is no low- Y_e ejecta, and the infrared emission is simply the long wavelength tail of the thermal spectrum that peaks in the optical. Such infrared light curves display two distinct maxima, separated by about 10 days. The origin of

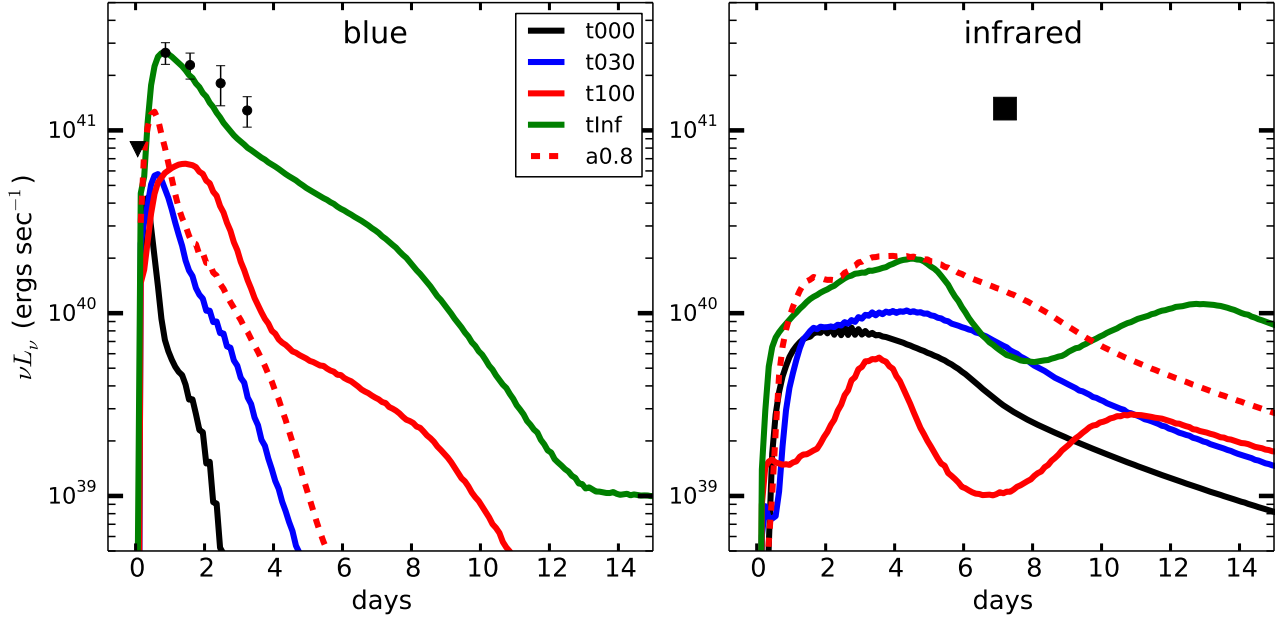


Figure 5. *Left Panel:* Angle averaged synthetic light curves of various wind models at optical blue wavelengths (3500 – 5000 Å). The closed circles show r-band observations of the possible kilonova following GRB 080503 (Perley et al. 2009). The triangle symbol denotes an upper limit. As the redshift of 080503 is unknown, we adopt a value $z = 0.25$ and neglect k-correction effects. *Right Panel:* Model light curves of the same models at infrared wavelengths (1 – 3 μm). The square shows the Hubble Space Telescope observations of the possible kilonova associated with GRB130603B (Tanvir et al. 2013; Berger et al. 2013).

the secondary maximum is similar to that studied for Type Ia SN, and results from an enhancement in infrared emissivity that occurs when the ejecta transitions from doubly to singly ionized (Kasen et al. 2006). The clear separation of the two maxima in these models may be an artifact of our approximate opacity prescription, which uses iron group atomic data as a proxy for all d-shell elements. In reality, the change in ionization state occurs at a different time for different elements, depending on the ionization potential. For complex mixtures, this may have the effect of smearing the two peaks together.

Figure 6 shows the spectra evolution of model t100 over 10 days. The color of the continuum rapidly evolves from blue emission produced in the outer high- Y_e layers of ejecta to infrared emission produced in the inner, low- Y_e ejecta. The spectra show numerous line absorption features that, given the moderate ejecta velocities (5000 – 10,000 km s $^{-1}$), are fairly well resolved. This differs from the spectra of dynamical ejecta, where the line features are highly blended due to the fast (0.1 – 0.3c) ejecta velocities (Kasen et al. 2013). However, given our approximate line opacities, the position of individual lines can not be trusted, and as line data from more species is added, line blending may become more prevalent. Although more work is needed to make quantitative spectral predictions, our results suggest that the relative slowness of the wind may be discernible in the line features, providing a way to distinguish a wind from dynamical ejecta. The presence of resolved lines also provides hope that the detailed composition of outflows could be estimated from spectral analysis.

3.3 Effect of Black Hole Spin

We have also considered one model, a0.8, in which the central remnant immediately became a rapidly spinning BH with Kerr parameter $a = 0.8$. The BH spin leads to a deeper potential well and a higher neutrino irradiation from the inner regions of the disk. The fraction of high- Y_e material in the wind is therefore greater than it is in the non-spinning prompt BH model t000. The amount of high and low- Y_e material ejected in model a.08 turns out to be comparable to the case of a HMNS with lifetime $t_{\text{ns}} = 30$ ms. As seen in Figure 5, the blue and infrared light curves of models a0.8 and t030 are indeed quite similar. This degeneracy represents a challenge in using kilonova observations to diagnose the lifetime of a HMNS.

3.4 Effect of Dynamical Ejecta

Prior to the ejection of disk winds, neutron rich material may be dynamically expelled in the merger, producing an overlying layer of rapidly expanding, presumably low- Y_e material. This dynamical ejecta may act as a “lanthanide curtain”, obscuring our view of the optical emission originating with the wind ejecta.

To explore this effect, we created several models in which we superimposed a spherical shell of $Y_e < 0.25$ material onto the outer region of the 2D wind model t100. We took the radial density profile of the shell to be a gaussian with central velocity $v = 0.2c$ and a width of $\Delta v = 0.1c$ and varied the mass of dynamical ejecta between $M_{\text{dyn}} = 10^{-5}$ and $10^{-2} M_\odot$.

Figure 7 shows the angle-averaged light curves for models with different values of M_{dyn} . Due to the extremely

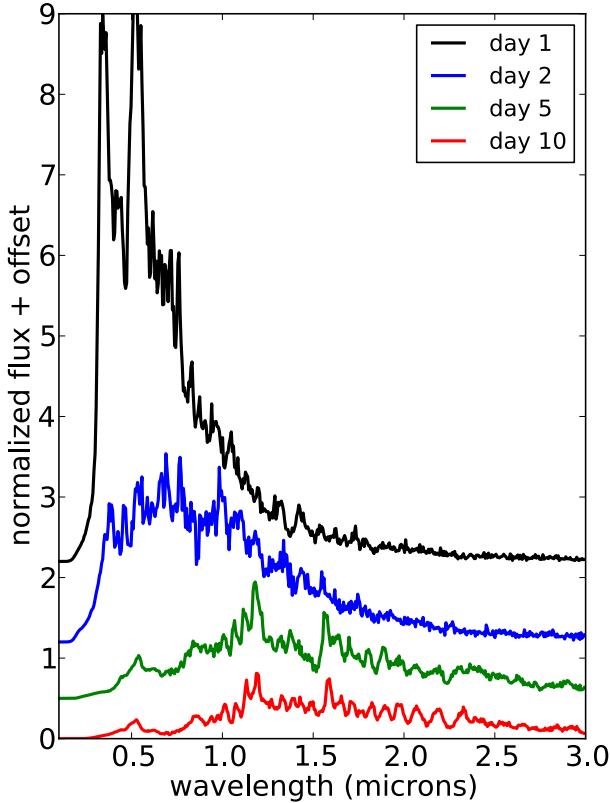


Figure 6. Spectral time series of model t100. The spectrum at early times ($t \lesssim 2$ days) is dominated by optical emission from the lanthanide-free, outer layers of the wind. At later times, the emission is dominated by infrared emission from lanthanide-rich material in the central wind regions. Relatively narrow line features ($v \approx 5000 \text{ km s}^{-1}$) are distinguishable however, due to the uncertainties in the atomic data, the positions of these features are not reliable.

high lanthanide opacities, we find that only a small mass of dynamical ejecta ($M_{\text{dyn}} \approx 10^{-4} M_{\odot}$) is required to suppress the blue optical flux by more than an order of magnitude. For models with $M_{\text{dyn}} \gtrsim 10^{-3} M_{\odot}$, the wind emission is completely invisible, and the optical and infrared light curves arise entirely within the dynamical ejecta. In these cases, the brief peak and subsequent tail of blue flux are due to the small fraction of optical radiation that is produced in and manages to escape from the heavily line-blanketed dynamical ejecta.

In realistic merger simulations, the dynamical ejecta is not completely spherical, and may possess some lanthanide-free “windows” through which we can see the wind ejecta. In the NS + NS simulations of Bauswein et al. (2013), the outflows have a torus-like anisotropy, with less material ejected along the polar axis. Neutrino irradiation of the dynamical ejecta may also raise the Y_e in the polar region, reducing the abundance of lanthanides in that material (Wanajo et al. 2014). In BH-NS mergers, mass ejection occurs mainly through the tidal tail of the NS, and forms a single thick arm confined to the equatorial plane.

To explore the possible geometrical effects, we constructed an additional model in which $M_{\text{dyn}} = 10^{-3}$ of dynamical ejecta was distributed in a torus about the equa-

torial plane. Here we took the density profile in both the r and z directions to be gaussian with width of $\Delta v = 0.1c$, a distribution that closely resembles the ejecta seen in the Newtonian NS-NS simulations of Rosswog (2005). Figure 8 shows the resulting light curves as seen from different viewing angles. For pole-on orientations ($\theta = 0^\circ$), an observer can see most of the wind ejecta through the hole of the dynamical torus, and the blue optical flux is only reduced by factor of ~ 2 at peak. For orientations closer to edge-on ($\theta = 90^\circ$), however, the dynamical torus obscures the wind optical flux by an order of magnitude or more.

3.5 Comparison to Observations

One week following the gamma-ray burst (GRB) 130603B, Tanvir et al. (2013) and Berger et al. (2013) detected an excess infrared emission that they attributed to a kilonova. In the right panel of Figure 5, we compare that *Hubble Space Telescope* infrared data point to our models. The luminosity of the 130603B excess is a factor of ~ 5 higher than the peak of even our brightest disk wind models. Since the peak luminosity is proportional to the square root of the ejecta mass, fitting the GRB 130603B infrared excess appears to require an ejecta mass of $\sim 0.1 M_{\odot}$, a factor of ~ 20 times higher than that ejected in any of our models.

Disk winds could explain the large ejecta mass inferred for GRB 130603B if we assume that the accretion disk was of higher initial mass, say $\sim 0.1 - 0.3 M_{\odot}$, rather the value $0.03 M_{\odot}$ adopted in our calculations. In addition, most of our models assumed a non-spinning black hole, whereas a rapidly spinning black hole can increase the wind ejecta mass by a factor of ~ 5 (Just et al. 2014; Fernández et al. 2014). Dynamical ejecta may also contribute to the infrared emission. A mass of $\sim 0.1 M_{\odot}$ is likely too large to come solely from the dynamical ejecta of a NS-NS merger, but it might be expelled in the merger between a NS and a low mass BH (Tanaka et al. 2014).

The left panel of Figure 5 compares our blue optical light curves to a different possible kilonova candidate, the optical “bump” that followed GRB 080503 (Perley et al. 2009). This event possessed no clear host galaxy and so we have chosen a redshift $z = 0.25$ to place the observations at a similar brightness to our models. The light curves of disk wind model with a long lived HMNS (e.g., tInf) fit the data reasonably well. A wind model that ejected ~ 4 times more mass would likely better fit the slower observed light curve decline, and would place the kilonova at the redshift $z = 0.56$, which corresponds to a faint spiral galaxy within the field of 080503 (a strong natal kick of the binary would be required to explain its large observed spatial offset in this case). GRB 080503 was accompanied by extremely bright extended prompt X-ray emission, which Metzger et al. (2008) speculate is powered by a stable magnetar created during a NS-NS merger (see also Bucciantini et al. 2012, Rezzolla & Kumar 2014). In this case, the kilonova emission could be significantly enhanced by rotational energy injected by the magnetized remnant (Yu et al. 2013; Metzger & Piro 2013).

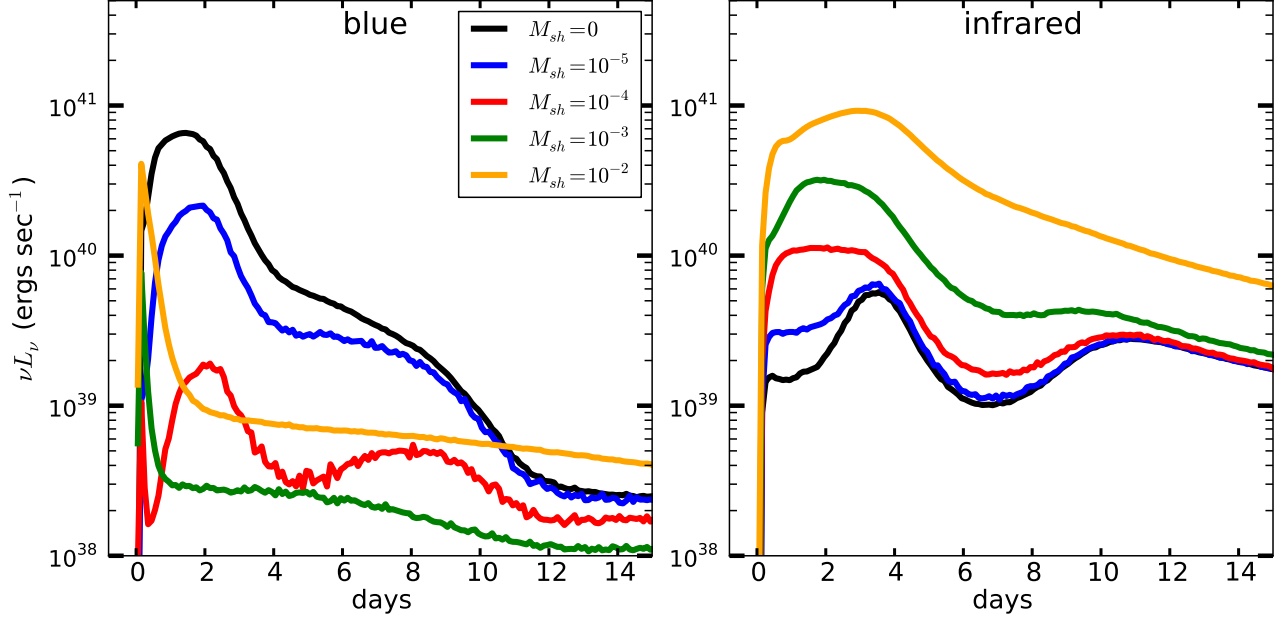


Figure 7. Angle averaged model light curves at optical blue wavelengths (left panel) and infrared wavelengths (right panel) for model t100 surrounded by a varying amount of spherically distributed dynamical ejecta. Only a small amount ($\sim 10^{-4} M_{\odot}$) of low- Y_e dynamical ejecta is needed to obscure the optical emission from the wind.

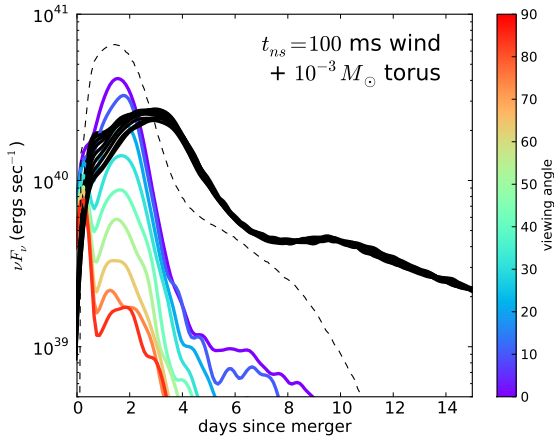


Figure 8. Synthetic light curves of wind model t100 surrounded by a $10^{-3} M_{\odot}$ torus of heavy r-process elements. Colored lines denote the optical blue (3500 – 5000 Å) light curve as seen from different viewing angles, while solid black lines denote the infrared light curve. The dashed black line shows the angle averaged blue light curve of model t100 when no dynamical ejecta is included. For pole on viewing angles ($\theta \approx 0^\circ$) the blue emission is visible through the hole in the torus, but for edge on orientations ($\theta \approx 90^\circ$), the dynamical ejecta suppresses the optical flux.

4 SUMMARY AND CONCLUSIONS

We have shown how material ejected in disk winds subsequent to a compact object merger can give rise to both optical and infrared kilonova emission. We studied the dependences on key parameters such as the delay until black hole formation, black hole spin, and the presence of neutron-rich dynamical ejecta. In Figure 9, we summarize

schematically the range of possible kilonova properties, and illustrate how they roughly map to the progenitor binary and remnant type. Our main findings are as follows:

1. – For the characteristic entropies and expansion times of disk winds, we find that the abundance of lanthanides cuts off sharply when the electron fraction $Y_e \gtrsim 0.25$ (Fig. 3). The electron fraction in turn is very sensitive to the level of neutrino irradiation of the wind and hence acts as a diagnostic of the physical conditions in the aftermath of the merger (Metzger & Fernández 2014).
2. – The presence of optical emission is a ubiquitous feature of the disk wind ejecta, even in the case of non-spinning, promptly-formed black hole remnants (Fig. 4). The magnitude and duration of this optical component is a sensitive function of the lifetime of a HMNS or the spin of the promptly-formed BH. In the limit of a very long-lived HMNS, photons emerge primarily in the optical, reaching luminosities up to 10^{41} erg s $^{-1}$ for moderate disk masses ($0.03 M_{\odot}$).
3. – The ratio of the optical to infrared luminosity from a kilonova provides a powerful measure of the relative mass of high- Y_e to low- Y_e ejecta. Using this information to infer the underlying physical scenario, however, may be difficult given the degeneracies. For example, the wind ejecta from a promptly-formed, rapidly spinning BH produces a similar kilonova light curve to that of a long-lived HMNS (Figure 5).
4. – Because the expansion velocities of the wind are moderate ($\sim 10,000$ km s $^{-1}$), numerous line absorption features are discernible in the spectra (Fig. 6). This distinguishes the spectra of disk winds from those of fast moving

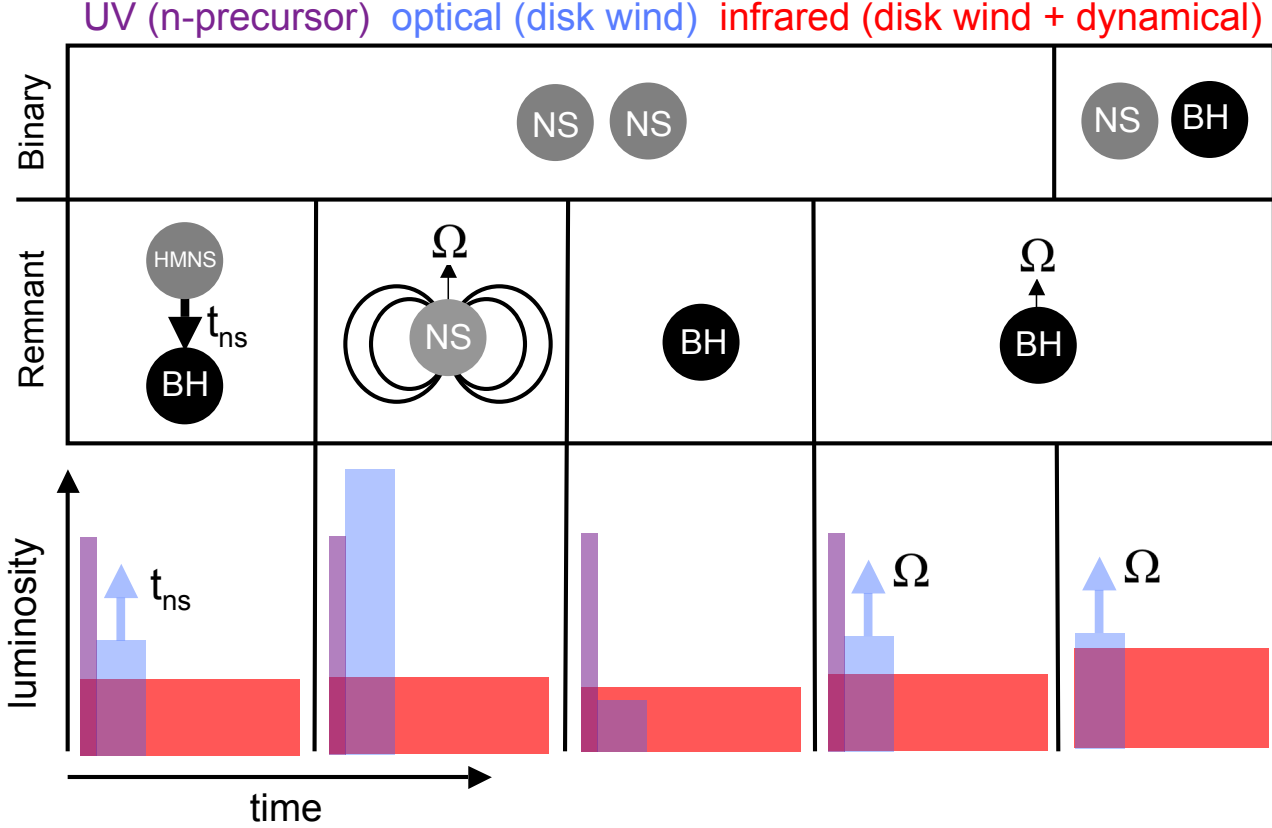


Figure 9. Schematic illustration of the mapping between mergers and kilonova light curves. The top panel shows the progenitor system, either a NS-NS or a NS-BH binary, while the middle plane shows the final merger remnant (from left to right: a HMNS that collapses to a BH after time t_{ns} , a spinning magnetized NS, a non-spinning BH, and a rapidly spinning BH). The bottom panel illustrates the relative amount of UV/blue emission from a n-precursor (purple), optical emission from lanthanide-free material (blue), and IR emission from lanthanide containing ejecta (red).

dynamical ejecta, for which the line features are broader and heavily blended. Observing the spectra of wind ejecta may thus allow us to study the detailed composition of freshly produced r-process material. At present, however, the atomic data is not good enough to predict all line wavelengths, and additional atomic structure calculations are needed.

5. – The optical emission from a disk wind can be easily obscured by even a small amount ($10^{-4} M_{\odot}$) of neutron-rich dynamical ejecta, causing most of the flux to emerge in the near infrared. In the case of NS-NS mergers, this dynamical ejecta is expected to be nearly isotropic, reducing the likelihood of observing an optical component (Fig. 7). For BH-NS mergers, the confinement of the dynamical ejecta to the equatorial plane makes the detection of optical emission possible from polar viewing angles (Fig. 8).

6. – The infrared emission excess observed following GRB 130603B can be explained by a disk wind only if the merger formed a rather massive disk ($\sim 0.1 M_{\odot}$). The optical bump observed following GRB 080503 (with a redshift of $z = 0.25 - 0.5$) can be nicely explained by a wind from a moderately massive disk ($\sim 0.03 M_{\odot}$) irradiated by

a long-lived HMNS.

Our calculations have illustrated the key properties of kilonova from disk winds, however several improvements are needed to generate reliable, quantitative theoretical predictions. On the wind dynamics side, a more advanced neutrino transport scheme is required to better quantify the distribution of electron fraction in the ejecta. Inclusion of magneto-hydrodynamics and general relativity is also important to quantify the amount of ejected mass. Using more realistic initial conditions, taken from an actual merger simulation, would provide a better description of the relative size and spatial distribution of the dynamical ejecta and accretion disk. Determining the detailed final composition of the wind requires post-processing wind tracer particles with nuclear reaction networks. On the radiative transport side, better line data for the high-Z elements, in particular the lanthanides and actinides, is necessary to calculate the pseudo-continuum opacity and line features. We also need a better understanding of the radioactive decay energy rate, and the thermalization of decay products (electrons, gamma-rays, and fission fragments). Our future work will take steps along these lines, with the hope of developing more realistic kilonova models.

ACKNOWLEDGMENTS

DK is supported in part by a Department of Energy Office of Nuclear Physics Early Career Award, and by the Director, Office of Energy Research, Office of High Energy and Nuclear Physics, Divisions of Nuclear Physics, of the U.S. Department of Energy under Contract No. DE-AC02-05CH11231. RF was supported by NSF Division of Astronomical Sciences collaborative research grant AST-1206097, and a UC Office of the President grant. BDM gratefully acknowledges support from the NSF grant AST-1410950 and the Alfred P. Sloan Foundation. This work was supported in part by NSF Grant No. PHYS-1066293 and the hospitality of the Aspen Center for Physics. The software used in this work was in part developed by the DOE NNSA-ASC OASCR Flash Center at the University of Chicago. We are grateful for computing time made available by the National Energy Research Scientific Computing Center, which is supported by the Office of Science of the U.S. Department of Energy under Contract No. DE-AC02-05CH11231. Computations were performed using *Carver* and *Hopper*.

REFERENCES

- Artemova I. V., Bjoernsson G., Novikov I. D., 1996, *ApJ*, 461, 565
- Barnes J., Kasen D., 2013, *ApJ*, 775, 18
- Bauswein A., Baumgarte T. W., Janka H.-T., 2013, *Physical Review Letters*, 111, 131101
- Beloborodov A. M., 2008, in Axelsson M., ed., *American Institute of Physics Conference Series Vol. 1054 of American Institute of Physics Conference Series, Hyper-accreting black holes*. pp 51–70
- Berger E., Fong W., Chornock R., 2013, *ApJL*, 774, L23
- Bucciantini N., Metzger B. D., Thompson T. A., Quataert E., 2012, *MNRAS*, 419, 1537
- Dubey A., Antypas K., Ganapathy M. K., Reid L. B., Riley K., Sheeler D., Siegel A., Weide K., 2009, *J. Par. Comp.*, 35, 512
- Duez M. D., Foucart F., Kidder L. E., Ott C. D., Teukolsky S. A., 2010, *Classical and Quantum Gravity*, 27, 114106
- Eichler M., Arcones A., Kelic A., Korobkin O., Langanke K., Martínez-Pinedo G., Panov I. V., Rauscher T., Rosswog S., Winteler C., Zinner N. T., Thielemann F.-K., 2014, *ArXiv e-prints*
- Fernández R., 2012, *ApJ*, 749, 142
- Fernández R., Kasen D., Metzger B. D., Quataert E., 2014, *MNRAS*, in press, *arXiv:1409.4426*
- Fernández R., Metzger B. D., 2013a, *MNRAS*, 435, 502
- Fernández R., Metzger B. D., 2013b, *ApJ*, 763, 108
- Freiburghaus C., Rosswog S., Thielemann F., 1999, *ApJ*, 525, L121
- Goriely S., Bauswein A., Janka H.-T., 2011, *ApJ*, 738, L32
- Grossman D., Korobkin O., Rosswog S., Piran T., 2014, *MNRAS*, 439, 757
- Hotokezaka K., Kiuchi K., Kyutoku K., Okawa H., Sekiguchi Y.-i., Shibata M., Taniguchi K., 2013, *Phys. Rev. D*, 87, 024001
- Just O., Bauswein A., Ardevol Pulpillo R., Goriely S., Janka H.-T., 2014, *MNRAS*, submitted, *arXiv:1406.2687*
- Kasen D., Badnell N. R., Barnes J., 2013, *ApJ*, 774, 25
- Kasen D., Thomas R. C., Nugent P., 2006, *ApJ*, 651, 366
- Kulkarni S. R., 2005, preprint, *arXiv:astro-ph/0510256*
- Kurucz R. L., Bell B., 1995, *Atomic line list*, CD-ROM, Cambridge, MA: Smithsonian Astrophysical Observatory
- Lattimer J. M., Schramm D. N., 1974, *ApJ*, 192, L145
- Lee W. H., Ramirez-Ruiz E., López-Cámara D., 2009, *ApJ*, 699, L93
- Li L., Paczyński B., 1998, *ApJ*, 507, L59
- Metzger B. D., Bauswein A., Goriely S., Kasen D., 2014, *ArXiv e-prints*
- Metzger B. D., Berger E., 2012, *ApJ*, 746, 48
- Metzger B. D., Fernández R., 2014, *MNRAS*, 441, 3444
- Metzger B. D., Martínez-Pinedo G., Darbha S., Quataert E., Arcones A., Kasen D., Thomas R., Nugent P., Panov I. V., Zinner N. T., 2010, *MNRAS*, 406, 2650
- Metzger B. D., Piro A. L., 2013, *MNRAS*, submitted, *arXiv:1311.1519*
- Metzger B. D., Piro A. L., Quataert E., 2008, *MNRAS*, 390, 781
- Metzger B. D., Piro A. L., Quataert E., 2009, *MNRAS*, 396, 304
- Metzger B. D., Quataert E., Thompson T. A., 2008, *MNRAS*, 385, 1455
- Nissanke S., Kasliwal M., Georgieva A., 2013, *ApJ*, 767, 124
- Paczynski B., Wiita P. J., 1980, *A&A*, 88, 23
- Perego A., Rosswog S., Cabezon R. M., Korobkin O., Käppeli R., Arcones A., Liebendörfer M., 2014, *MNRAS*, 443, 3134
- Perley D. A., et al., 2009, *ApJ*, 696, 1871
- Piran T., Korobkin O., Rosswog S., 2014, *arXiv:1401.2166*
- Piran T., Nakar E., Rosswog S., 2013, *MNRAS*, 430, 2121
- Rezzolla L., Kumar P., 2014, preprint, *arXiv:1410.8560*
- Roberts L. F., Kasen D., Lee W. H., Ramirez-Ruiz E., 2011, *ApJ*, 736, L21+
- Rosswog S., 2005, *ApJ*, 634, 1202
- Shakura N. I., Sunyaev R. A., 1973, *A&A*, 24, 337
- Surman R., McLaughlin G. C., Hix W. R., 2006, *ApJ*, 643, 1057
- Tanaka M., Hotokezaka K., 2013, *ApJ*, 775, 113
- Tanaka M., Hotokezaka K., Kyutoku K., Wanajo S., Kiuchi K., Sekiguchi Y., Shibata M., 2014, *ApJ*, 780, 31
- Tanvir N. R., Levan A. J., Fruchter A. S., Hjorth J., Hounsell R. A., Wiersema K., Tunnicliffe R. L., 2013, *Nature*, 500, 547
- Timmes F. X., 1999, *ApJ Supplements*, 124, 241
- Timmes F. X., Swesty F. D., 2000, *ApJS*, 126, 501
- Wanajo S., Sekiguchi Y., Nishimura N., Kiuchi K., Kyutoku K., Shibata M., 2014, *ApJL*, 789, L39
- Yu Y.-W., Zhang B., Gao H., 2013, *ApJL*, 776, L40